

An Approach to Gamma-Hadron Separation via Measurements of the Middle-UV Fraction of EAS emission by an Imaging Atmospheric Cherenkov Telescope with UV-Sensitive SiPM detectors

E.E. Kholupenko¹, D.V. Badmaev¹, N.M. Budnev², A.M. Bykov¹, A.M. Krassilchtchikov¹, L.A. Kuzmichev^{2,3}, A.A. Bogdanov¹, Yu.V. Chichagov¹, G.A. Repman¹ and Yu.V. Tuboltsev¹

¹ Ioffe Institute, Saint-Petersburg, Russian Federation; *eugene@astro.ioffe.ru*

² Irkutsk State University, ISU, Irkutsk, Russian Federation

³ Skobeltsyn Institute of Nuclear Physics, MSU, Moscow, Russian Federation

Received 20xx month day; accepted 20xx month day

Abstract The operation of a small-size Cherenkov gamma-ray telescope TAIGA-IACT with camera on SiPMs OnSemi MicroFJ-60035 has been modelled by multiparticle Monte Carlo (MC) methods. The model implies that telescope camera is equipped with two specific types of filters of 290 – 590 nm (visible+NUV) and 220 – 320 nm (MUV+UVB)-bands, each covering half of the camera pixels in some uniform order. This allows one to measure the fraction of UV-radiation in total amount of Cherenkov radiation of an extensive air shower (EAS), that can be used for efficient gamma-hadron separation. The corresponding quality factor takes values up to 5.07 in the 10 – 100 TeV range depending on the distance to EAS axis and camera orientation.

Key words: extensive air showers, gamma-hadron separation, (gamma-hadron selection), Cherenkov gamma-ray telescopes, middle UV band

1 INTRODUCTION

In recent decades Cherenkov gamma-ray astronomy has demonstrated a rapid development (e.g., Bykov et al. 2017 and references therein): the maximal size of telescope mirrors has significantly increased (from 0.9 m (Fegan et al. 1968) to 28 m (Gottschall et al. 2015)), the employed photosensors are substantially improved (in particular, older photo-multiplier tubes are replaced by newer PMTs with higher efficiency (e.g. Hanna et al. 2022)), the number of telescopes and detector units operating together within a single observatory has increased from a single standalone imaging atmospheric telescope (e.g., Whipple (Weekes et al. 1989)) to observatories consisting of multiple IACTs and muon detectors (e.g. HEGRA (Aharonian

et al. 2008), H.E.S.S. II (Hofmann & H. E. S. S. Collaboration 2003), TAIGA (Budnev et al. 2022)). The largest of currently developed gamma-ray and cosmic ray observatories will consist of several tens of IACTs (e.g. CTA (Longo 2022)). Such a development has already allowed specialists to achieve very impressive results in observation of cosmic gamma-ray sources (e.g. van Eldik et al. 2015; Ansoldi et al. 2016). These results are based not only on technical improvements, but also on development of data analysis techniques: from simple measuring of gamma-ray signal excess above the cosmic ray background (e.g. Charman 1969) to analysis of Hillas parameters (Hillas 1985; Weekes et al. 1989), multifractal and wavelet moments (e.g. Razdan et al. 2002 and references therein), time- (e.g. Aharonian et al. 1997; Razdan et al. 2002) and spectral parameters (e.g. Stepanian et al. 1983; Rahman et al. 2001) and further to analysis involving neural networks (e.g. Bussino & Mari 2001; Razdan et al. 2002; Postnikov et al. 2018 and references therein).

At the same time, some of the developed techniques of observations and data analysis in Cherenkov gamma-ray astronomy yet have not become widespread, probably due to relative complexity of realization and application in comparison with other competing technologies employed to solve same problems, or to incapability of the existed equipment to ensure their effective employment in full degree. One of such techniques is measurement of the fraction of ultraviolet (UV) radiation in the total amount of extensive air shower (EAS) Cherenkov radiation. This method can be used to perform gamma-hadron separation of the shower primaries (hereinafter “UV gamma-hadron separation”), which is an essential step in data analysis. The approach is based on the fact that this fraction for the EASs induced by cosmic ray (CR) protons is larger than for the EASs induced by gamma-quanta, because generation of EAS Cherenkov radiation by CR protons in the atmosphere occurs deeper (on average) than in the case of EASs from gamma-quanta. Thus, the EAS Cherenkov photons from CR protons propagate to the registration point through a smaller optical depth of the atmospheric ozone (and, correspondingly, are less absorbed, that is essential in the UV band) in comparison with ones from gamma-quanta (for a detailed consideration of this effect, see Aharonian et al. 1997; Rahman et al. 2001; Razdan et al. 2002; Kholupenko et al. 2018 and references therein). This, in turn, leads to formation of EAS Cherenkov radiation spectra which have significantly different shapes in UV-range (especially, in MUV-range) for EASs induced by gamma-quanta and protons (see Fig. 1). For the first time the said technique was proposed by Stepanian et al. (1983), tested (Zyskin et al. 1987) and employed for registration of cosmic gamma-ray sources (e.g. Kalekin et al. 1995; Neshpor et al. 2001) at the GT-48 Cherenkov telescope. The cameras of GT-48 telescopes (as well as other Cherenkov telescopes of the first three generations¹) were based on vacuum photo-multipliers (PMTs): PMTs of the visible band (300 – 600 nm) were used to register the main part of EAS Cherenkov radiation, while the PMTs of the middle-UV band (200 – 300 nm) were used to register the UV emission of the EAS.

One of the main changes being carried out in Cherenkov telescopes of the new (IV) generation, is the extensive use of silicon photo-multipliers (SiPMs) instead of vacuum PMTs as camera photo-detectors. After the successful operation of FACT (Knoetig et al. 2013; Bretz et al. 2014), several SiPM cameras were proposed and developed (see e.g. Lombardi et al. 2020; Adams et al. 2021). In accordance with this tendency, a new SiPM-based camera for small-size Cherenkov telescopes TAIGA-IACT is being developed at the Ioffe Institute (e.g. Bogdanov et al. 2020, 2021a,b; Kuleshov et al. 2021; Bogdanov et al. 2022).

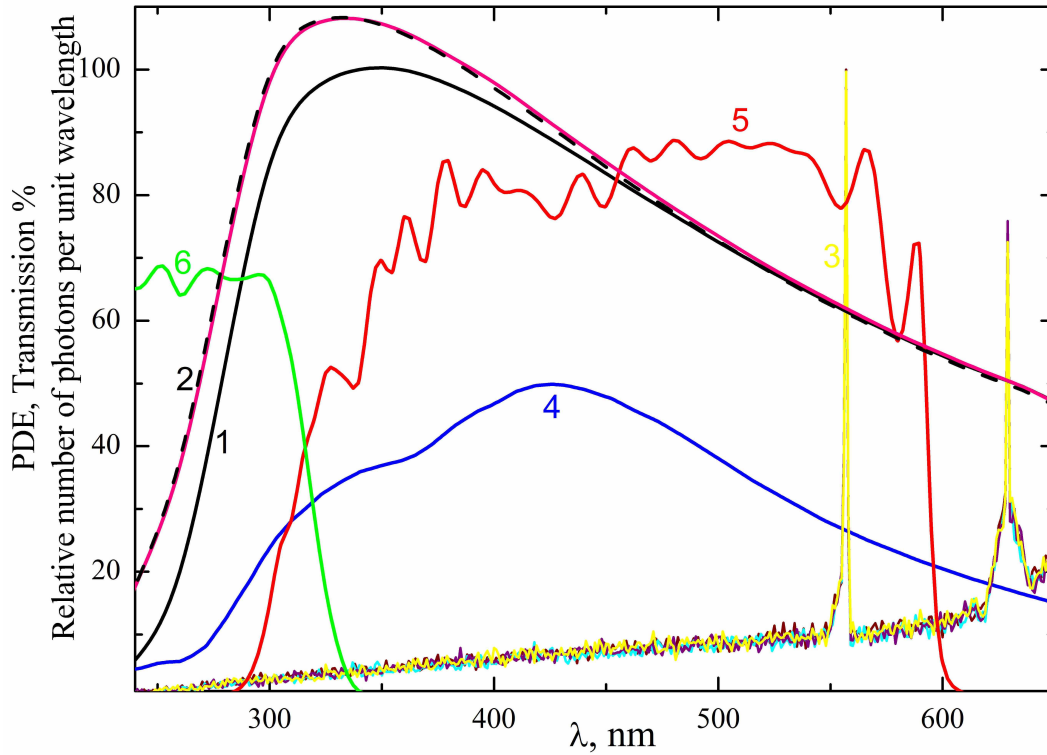


Figure 1: Dependencies of profiles on wavelength λ : 1) an averaged spectrum of Cherenkov radiation from EASs induced by 31.62 TeV gamma-quanta, normalized to 100% at maximum at $\simeq 340$ nm, is shown by the black solid curve; 2) averaged spectra of Cherenkov radiation from EASs induced by 31.62 TeV and 100 TeV protons, normalized such that to coincide asymptotically with averaged spectrum from γ -EASs at long wavelengths, are shown by pink solid and black dashed curves overlapped practically; 3) four specific realizations of the night sky background spectrum (normalized to 100% at maximum at $\simeq 557$ nm), simulated within a Monte Carlo approach using the data of Leinert et al. (1998); Benn & Ellison (1998); Mikhalev et al. (2001); Mikhalev & Medvedeva (2002), are shown by partially overlapped yellow, purple, cyan, and wine curves; 4) the photon detection efficiency of a OnSemi MicroFJ-60035 SiPM (ON-Semiconductor 2017), $PDE(\lambda)$, is shown by the blue curve; 5) the transmission coefficient of the optical band filter SL 290-590 (Zabudko 2021) is shown by the red curve; 6) the transmission coefficient of the 220-320 nm band NSH+KCSH filter (Manomenova et al. 2005; Rudneva et al. 2018) is shown by the green curve.

TAIGA-IACT is an array of Cherenkov telescopes developed as an essential part of the gamma-ray and cosmic ray observatory TAIGA located in the Tunka valley, Rep. of Buryatiya. The TAIGA observatory consists of a set of instruments of various types, including wide-angle integrated timing arrays Tunka-133 and HiSCORE, scintillation arrays Tunka-Grande and TAIGA-muon arrays (e.g Kuzmichev et al. 2018; Kuzmichev 2022; Budnev et al. 2022). In August 2022 an experimental cluster based on OnSemi MicroFJ-60035 SiPMs and optical filters SL 290 – 590 manufactured by Photoptic Ltd²(Zabudko 2021) has been installed into the camera of one of the TAIGA-IACT units (see Fig. 2) and underwent full-scale operation test. One of the features of OnSemi MicroFJ-60035 is a relatively wide-range PDE (at a 6 V overvoltage the $PDE \geq 10\%$ in the 275-700 nm interval (ON-Semiconductor 2017)). From one side, this requires usage



Figure 2: The front view (photosensitive side) of the TAIGA-IACT camera with an experimental SiPM cluster installed into camera in August 2022. Here the SiPM pixels of the experimental cluster (in the left side of camera) are covered by 290-590 nm band filters.

of optical filters (at least to avoid the influence of the optical noise sharply increasing at wavelengths above $\simeq 640$ nm due to the emission of atmospheric hydroxyl (OH) in the Meinel bands (e.g. Leinert et al. 1998; Benn & Ellison 1998, see Fig. 1). But from the other side, this feature opens a possibility to use the same photosensors for registration of the EAS Cherenkov radiation in the middle UV band³ and in the visible band by application of filters with different transmission bands (see Fig. 1). The pixels of a telescope camera can be masked with two types of filters placed in some uniform order keeping the “50%/50%” number ratio (e.g., Fig. 3). This would allow one to register simultaneously both the visible and the middle UV Cherenkov radiation from a particular flash (induced by a particular EAS) with one camera on a single standalone Cherenkov telescope, and thus, to perform gamma-hadron separation via a cut-off on the fraction of the middle UV band emission in the total flux of the measured Cherenkov flash emission. For suggested method of gamma-hadron separation the properties of (MUV+UVB)-filters are critically important while the properties of filters of main working range (visible + NUV) can vary in a wider range without significant worsening of efficiency of particle type discrimination. The key (MUV+UVB)-filter properties affecting gamma-hadron separation efficiency are the maximal transmission value and the transmission band $[\lambda_1, \lambda_2]$

³ The product of transmission of a (MUV+UVB)-band filter and the PDE of the chosen SiPM provides sensitivity in the 280-320 nm

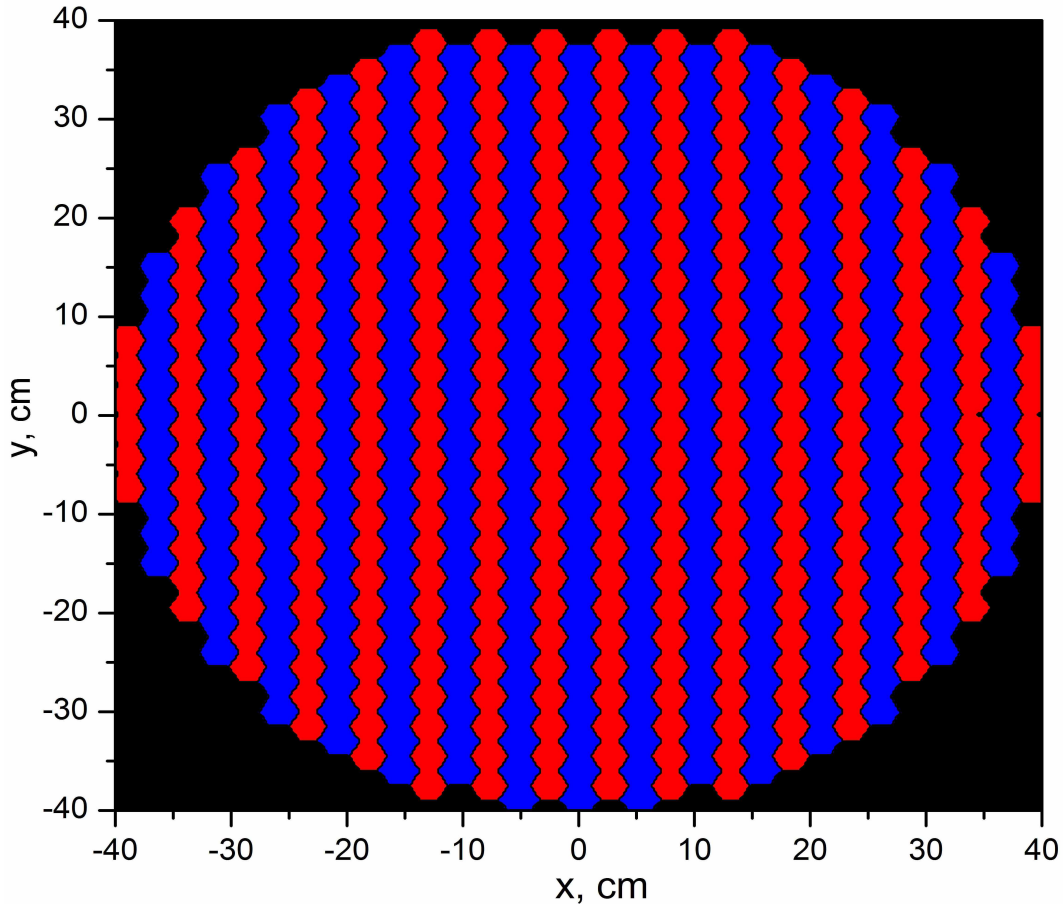


Figure 3: An example of camera filling pattern. Two types of filters are employed: the pixels masked by (UVB+MUV) band (220-320 nm) filters are shown in red, the pixels masked by (visible+NUV) band (290-590 nm) filters are shown in blue.

(usually defined at a half of maximal transmission). The transmission values within this band should be as high as possible to provide the maximal level of signal, because the energy threshold to apply UV gamma-hadron separation is approximately inversely proportional to registration efficiency in (MUV+UVB)-range (*ceteris paribus*). The upper (longwavelength) limit λ_2 of transmission band should be in the interval of about $\sim 300 - 320$ nm, where, from one side, the EAS Cherenkov spectrum is already sensitive to the primary particle type (see Fig. 1), and, from the other side, the number of EAS Cherenkov photons is still enough to be registered successfully. The lower (shortwavelength) limit λ_1 of transmission band should provide a large enough width $(\lambda_2 - \lambda_1) \gtrsim 40$ nm of transmission band to register the maximal number of (MUV+UVB) EAS Cherenkov photons (*ceteris paribus*). An attempt to use filters with transmission band in other parts of UV-range will make UV gamma-hadron separation quite ineffective: in UVA-range the spectrum shape is much less sensitive to the particle type (see Fig. 1) than needed, while in the most part of UVC-range the number of EAS Cherenkov photons becomes too small to be registered efficiently (see Fig. 1).

The present paper is devoted to investigation of efficiency of a TAIGA-IACT unit with an upgraded camera based on OnSemi MicroFJ-60035 SiPMs in regards of gamma-hadron separation carried out by

Previously, such an efficiency was estimated only in some general terms (Rahman et al. 2001, 2002; Kholupenko et al. 2018, 2022) and the calculated quantities were not the ones that can be directly measured. For example, in Razdan et al. (2002) the main characteristics of the gamma-hadron separation efficiency (the quality factor) remained indeterminate. Specific conditions considered in Rahman et al. (2001, 2002); Razdan et al. (2002); Kholupenko et al. (2018) also were different from conditions of the TAIGA observatory. In the present paper all the values are connected to measurable quantities, and the overall separation efficiency is estimated in general terms (similar to Rahman et al. (2001, 2002); Kholupenko et al. (2018)) and, finally, in the commonly accepted terms of the quality factor. The considered conditions are specific for TAIGA-IACT, however similar calculations can be carried out for any of the currently operating or planned IACTs. The calculations are based on multi-particle Monte Carlo simulations described in Sec. 2.

2 MONTE CARLO SIMULATIONS OF EAS DEVELOPMENT AND EMISSION

Formation and propagation of Cherenkov emission from extensive air showers (EASs) was modelled with the CORSIKA 7.7400 package (Heck et al. 1998), which is the most used tool for modeling of EASs, often considered a reference for other codes employed for this purpose.

The initial conditions (setup) for the modeling we have carried out, were the following. The primary particles were 10, 31.62, and 100 TeV gamma-quanta and 31.62, 100, and 316.2 TeV protons. The energies of protons differed by the factor of $10^{0.5}$ for the following reason: the Cherenkov emission images of events from CR protons are weaker (i.e., have less $Size^4$) by a factor of $\sim 1.5 - \sim 3$ than those from gamma-quanta of the same energy. Thus, images of EAS events from 31.62 TeV protons have the same average \overline{Size} (which is a measured parameter) as images of events from gamma-quanta with energies in the [10, 31.62] TeV interval (the exact value depends of a number of other factors, for details see Sec. 3). The angle of incidence (the zenith angle, Θ) of the primary particles was fixed at 40° . The direction of propagation of the primary particles was from South-to-North (X-axis; these conditions roughly imitate gamma-ray emission from the Crab Nebula as seen at the TAIGA observatory at its culmination). The telescope positions were [-180, -150, -120, -90, 0, 90, 120, 150, 180] m along X-axis (with Y=0 m) and [0, 90, 120, 150, 180] m along Y-axis (with X=0 m). The magnetic field strength was fixed at (H,Z)=(18.5, 57.7) μT (e.g. Thébault et al. 2015). The observation altitude at TAIGA is 675 m a.s.l. (Vasiliev et al. 2009), the corresponding atmosphere depth is $\simeq 950 - 960 \text{ g}\cdot\text{cm}^{-3}$. The atmosphere model was N3, winter middle-latitude (Kneizys et al. 1996). The considered wavelength range of the Cherenkov photons was 200-700 nm. The bunch size (CERSIZ parameter of CORSIKA) was 1 photon. A typical shape of EAS Cherenkov spectrum is shown in Fig. 1.

Monte Carlo simulations of the night sky background (NSB) were performed with the TAIGA Soft package (Kholupenko et al. 2022). The functional dependence of a smoothed and averaged NSB spectrum \bar{I}_λ on the wavelength λ is based on the data from Leinert et al. (1998). Additional spectral features taken into account in the NSB simulations are the atomic oxygen line at 557.7 nm and the doublet at {630.2 nm and 636.4 nm} (approximately simulated as a line with a significantly broadened base). These lines are the most bright emission features of the night atmosphere in the 200-700 nm band (Benn & Ellison 1998;

⁴ In Cherenkov astronomy, the *Size* of a triggered event is the sum of the time-integrated signal in all the camera pixels, which are

Mikhalev et al. 2001; Mikhalev & Medvedeva 2002). The increasing trend in the $\gtrsim 640$ nm band imitates emission of the atmospheric hydroxyl (OH) in the Meinel bands (Leinert et al. 1998; Benn & Ellison 1998). The total intensity is normalized to $I = \int I_\lambda d\lambda = 3 \cdot 10^{12}$ photon·m⁻²s⁻¹ster⁻¹ in the 300-600 nm band based on the data of the TAIGA-IACT team (Kuzmichev et al. 2018), that is in good accordance with the data of Mirzoyan & Lorenz (1994) for a wide-angle detector (i.e. with the field of view $\gg 1^\circ$).

The telescope unit parameters employed for the modeling were as follows: the field of view is 9.72° ; the mirror consists of 34 segments of 60 cm diameter each (Lubsandorzhev et al. 2017), thus the total mirror area is $S_m \simeq 9.6$ m², the radius of the mirror mechanical construction is $R_T \simeq 2.15$ m; the focal length is 4.75 m; the mirror albedo (the reflectivity coefficient) is 0.8; the transmission coefficient of the cover glass is 0.9; the transmission curves of the optical filters of main working range SL 290 – 590 (Zabudko 2021) and (MUV+UVB)-range NSH+KCSH (Manomenova et al. 2005; Rudneva et al. 2018) are as shown in Fig. 1; the considered filter mask is shown in Fig. 3; the Winston cone transmission is 0.7 (this conservative estimate is based on the calculations by Antonov et al. (2024)); the photon detection efficiency PDE (λ) of SiPM OnSemi MicroFJ-60035 ON-Semiconductor (2017) is presented in Fig. 1; the time frame of event registration is 15 ns.

Monte Carlo simulations of photon transport in the telescope and of event detection in its camera also were carried out by means of the TAIGA Soft package. All the details of the step-by-step algorithm realized in TAIGA Soft can be found in Kholupenko et al. (2022, 2024).

3 RESULTS AND DISCUSSION

Multiparticle Monte Carlo simulations of EAS emission as well as of the Cherenkov photon transport in the atmosphere and in the telescope optical system, carried out according to the approach and algorithms described in Kholupenko et al. (2022, 2020), were ultimately used to calculate the following ratio:

$$UV = \frac{\max\{I_u\}}{\max\{I_v\}}, \quad (1)$$

where I_i is the signal amplitude in pixel i (measured in photo-electrons [ph.e.]), the index u runs over the pixels masked by the (UVB+MUV) band filters (220-320 nm), while the index v runs over the pixels masked by (visible+NUV) band filters (290-590 nm).

In numerical modeling the UV -value is calculated as a function of primary particle energy and distance of registration (from EAS axis). In actual observations the particle energy is not measured directly but estimated by means of *Size* parameter which is total number of registered photoelectrons generated in camera by EAS Cherenkov radiation. The value of this parameter is approximately proportional to the particle energy but proportionality coefficient is different for primary gamma-quanta and CR protons and also depends on distance from the EAS axis to registration point. The correspondence (as exact as possible taking into account statistical nature of parameters) can be stated as a result of numerical modeling for specific telescope (i.e. this correspondence is unique for every cherenkov telescope). Thus the calculation allowing comparison of values of UV parameter for gamma-quanta and CR protons directly for the same values of *Size*, demands two stages: first, to determine the dependencies of mean \overline{Size} (and its mean-square-deviation) on particle energy for CR protons and gamma-quanta, and, second, to simulate events

from EAS axis. Such a calculation would require very large computer resources (processor time, RAM, and disk space). But general statement (for all types of cherenkov telescopes) about \overline{Size} relation is that for fixed value of particle energy E the corresponding proton parameter, $Size_p$, and gamma-quantum parameter, $Size_\gamma$, satisfy the following inequality:

$$\overline{Size}_\gamma(E/3) < \overline{Size}_p(E) < \overline{Size}_\gamma(E). \quad (2)$$

For considered configuration of TAIGA IACT (with the SiPM-camera and filters of 290-590 nm (visible+NUV) and 220-320 nm (UVB+MUV) bands), the validity of inequality (2) can be seen from comparison of data of Tab. 1 and Tab. 2 under assumption of monotonic continuous (approximately proportional) dependence of \overline{Size} from particle energy.

Table 1: Values of $\overline{Size} \pm \sigma_{Size}$ parameter [ph.e.] for γ primaries

Energy, TeV	10	31.62	100
(x, m; y, m)			
(-180; 0)	510 ± 73	1761 ± 218	6036 ± 653
(-150; 0)	516 ± 113	1869 ± 342	6671 ± 1081
(-120; 0)	462 ± 161	1813 ± 512	6906 ± 1692
(-90; 0)	330 ± 188	1422 ± 641	5942 ± 2321
(0; 0)	563 ± 267	2247 ± 1291	9351 ± 6134
(90; 0)	299 ± 172	1294 ± 599	5449 ± 2224
(120; 0)	422 ± 153	1673 ± 486	6371 ± 1587
(150; 0)	479 ± 107	1744 ± 320	6241 ± 995
(180; 0)	483 ± 70	1662 ± 201	5690 ± 592
(0; 0)	563 ± 267	2247 ± 1291	9351 ± 6134
(0; 90)	612 ± 191	2319 ± 656	8795 ± 2334
(0; 120)	667 ± 179	2488 ± 587	9139 ± 1831
(0; 150)	716 ± 134	2557 ± 384	8883 ± 949
(0; 180)	609 ± 47	2008 ± 115	6526 ± 216

The upper part of Tables 1 and 2 (as well as other tables in the paper) describes changes of investigated quantities along axis X (South→North), while the lower parts do changes of investigated quantities along axis Y (East→West). The point (0 m, 0 m) is included in tables twice for convenience.

There are several reasons leading to formation of complex two-dimensional (surface) distribution of \overline{Size} -parameter in XY-plane, in comparison with the simple axis-symmetric case of vertical incidence of primary particle without magnetic field. One of these reasons is of artificial origin (i.e. connected with specific equipment construction), while the others come from EAS physical nature. These reasons are the following:

1) Order of camera filling with filters is asymmetric relative to camera axes x and y (see Fig. 3): the filters

Table 2: Values of $\overline{Size} \pm \sigma_{Size}$ parameter [ph.e.] for proton primaries

Energy, TeV	31.62	100	316.2
(x, m; y, m)			
(-180; 0)	973 ± 273	3739 ± 852	13541 ± 2611
(-150; 0)	1077 ± 389	4236 ± 1268	15830 ± 4095
(-120; 0)	1137 ± 552	4642 ± 1992	17857 ± 6335
(-90; 0)	1112 ± 732	4687 ± 2835	18613 ± 8943
(0; 0)	2476 ± 5697	11473 ± 19084	51920 ± 55127
(90; 0)	1038 ± 678	4361 ± 2663	17295 ± 8386
(120; 0)	1054 ± 514	4322 ± 1872	16625 ± 5945
(150; 0)	1003 ± 363	3975 ± 1221	14805 ± 3844
(180; 0)	917 ± 258	3516 ± 797	12749 ± 2421
(0; 0)	2476 ± 5697	11473 ± 19084	51920 ± 55127
(0; 90)	1426 ± 720	5865 ± 2621	22732 ± 8511
(0; 120)	1364 ± 555	5486 ± 1816	20809 ± 5921
(0; 150)	1267 ± 400	4944 ± 1188	18078 ± 3397
(0; 180)	1035 ± 252	3786 ± 655	13243 ± 1716

Thus the images of the same EAS observed with offset along X-axis and Y-axis include different fractions of pixels masked by visible and MUV filters. This leads to significant asymmetry of surface \overline{Size} -distribution relative to placement of telescope (observation point) on different axes: \overline{Size} -values observed with offset along Y are larger than ones observed with offset along X by $\sim 1.1 - \sim 2$ times for gamma-quanta and by $\sim 1 - \sim 1.4$ times for protons depending on particle energy and distance from EAS axis. This ratio is different for gamma-quanta and protons because proton images are more scattered than gamma-quanta ones.

2) The presence of magnetic field of $\simeq 0.6$ Gs leads to deflection of trajectories of charged particles. Despite the fact that energy of considered primary particles are larger than 1 TeV, the most part of secondary electrons (and positrons) with energies above Cherenkov threshold (which are responsible for generation of Cherenkov photons) have energies less than ~ 1 GeV (see e.g. Giller et al. 2004). Corresponding Larmor radii are less than ~ 50 km and may be comparable with EAS length. This leads to significant asymmetry of angular distribution of EAS Cherenkov beam on azimuth angle (see e.g. Homola et al. 2015) and broadening of angular distribution in the direction perpendicular to geomagnetic field (see e.g. Cummings et al. 2021). This, in turn, leads to formation of “elliptical” profile of Cherenkov photon surface density⁵, broadened in the direction perpendicular to geomagnetic field (in our case, Y) with an additional contribution to eccentricity at the level of ~ 0.1 , which affects surface \overline{Size} -distribution correspondingly.

3) The observation plane (Earth surface) is not perpendicular to the EAS axis. This leads to formation of “elliptical” profile of Cherenkov photon surface density (in the same sense as in point 2)), broadened in the direction of inclination (in our case, X) with an additional contribution to eccentricity at the level of $\simeq \sin \Theta \simeq 0.64$, which affects surface \overline{Size} -distribution correspondingly.

4) The inclination of EAS leads to different values of slant depth on Rayleigh scattering for Cherenkov

photons coming to observation surface with positive and negative values of coordinate X . Corresponding contribution to relative difference between surface density (and \overline{Size}) in points X and $-X$ can be estimated as $\delta_R^S \simeq -2\Lambda_R X \sin \Theta$ (the upper index ‘‘S’’ stands for *Size*), where Λ_R is Rayleigh scattering coefficient near Earth surface, which takes values from $\simeq 10^{-5} \text{ m}^{-1}$ at 570 nm to $1.44 \cdot 10^{-4} \text{ m}^{-1}$ at 300 nm (see e.g. Bucholtz 1995). The relative difference, δ_R^S , may achieve $\sim -5\%$ for distant observation points $X = \pm 180$ m.

The asymmetry of surface \overline{Size} -distribution, arising from cumulative action of factors 1 – 4 listed above (together with other traditional difficulties of EAS physics), is difficult to be predicted precisely (at percent level) from general reasonings and simple analytical estimates.

The inequality (2) allows us to avoid two-stage calculation and to estimate the efficiency of UV gamma-hadron separation by consequent comparison of UV -parameters for events from CR protons of energy E_p with ones from gamma-quanta of energies $E_\gamma = E_p$ and $E_\gamma \simeq E_p/3$.

The simplest way to see the effectiveness of UV gamma-hadron separation is to compare the mean values of UV and its mean square deviations. These values at various distances from the EAS axis and for various energies of the primary particle are shown in Tab. 3 (for the gamma-quanta) and in Tab. 4 (for the cosmic ray protons).

Table 3: Mean values and mean square deviations of the UV -parameter for gamma-quanta

Energy, TeV	10	31.62	100
(x, m; y, m)			
(-180; 0)	$(3.25 \pm 1.56) \cdot 10^{-2}$	$(4.07 \pm 1.46) \cdot 10^{-2}$	$(4.76 \pm 1.1) \cdot 10^{-2}$
(-150; 0)	$(2.31 \pm 1.29) \cdot 10^{-2}$	$(2.78 \pm 1.21) \cdot 10^{-2}$	$(3.4 \pm 1.06) \cdot 10^{-2}$
(-120; 0)	$(2.16 \pm 0.95) \cdot 10^{-2}$	$(1.95 \pm 0.77) \cdot 10^{-2}$	$(2.3 \pm 0.82) \cdot 10^{-2}$
(-90; 0)	$(4.77 \pm 2.66) \cdot 10^{-2}$	$(3.83 \pm 1.53) \cdot 10^{-2}$	$(2.77 \pm 0.74) \cdot 10^{-2}$
(0; 0)	$(6.46 \pm 7.78) \cdot 10^{-3}$	$(5.93 \pm 2.97) \cdot 10^{-3}$	$(6.66 \pm 3.39) \cdot 10^{-3}$
(90; 0)	$(4.47 \pm 2.98) \cdot 10^{-2}$	$(4.35 \pm 1.76) \cdot 10^{-2}$	$(3.04 \pm 0.86) \cdot 10^{-2}$
(120; 0)	$(2.30 \pm 1.00) \cdot 10^{-2}$	$(1.90 \pm 0.70) \cdot 10^{-2}$	$(2.1 \pm 0.77) \cdot 10^{-2}$
(150; 0)	$(2.07 \pm 1.18) \cdot 10^{-2}$	$(2.51 \pm 1.19) \cdot 10^{-2}$	$(3.08 \pm 1.05) \cdot 10^{-2}$
(180; 0)	$(2.86 \pm 1.51) \cdot 10^{-2}$	$(3.62 \pm 1.42) \cdot 10^{-2}$	$(4.35 \pm 1.17) \cdot 10^{-2}$
(0; 0)	$(6.46 \pm 7.78) \cdot 10^{-3}$	$(5.93 \pm 2.97) \cdot 10^{-3}$	$(6.66 \pm 3.39) \cdot 10^{-3}$
(0; 90)	$(8.14 \pm 9.84) \cdot 10^{-3}$	$(5.55 \pm 1.77) \cdot 10^{-3}$	$(4.7 \pm 0.9) \cdot 10^{-3}$
(0; 120)	$(7.15 \pm 11.2) \cdot 10^{-3}$	$(3.9 \pm 1.59) \cdot 10^{-3}$	$(3.3 \pm 0.7) \cdot 10^{-3}$
(0; 150)	$(8.24 \pm 14.2) \cdot 10^{-3}$	$(3.71 \pm 2.56) \cdot 10^{-3}$	$(2.83 \pm 0.84) \cdot 10^{-3}$
(0; 180)	$(9.72 \pm 16.6) \cdot 10^{-3}$	$(5.24 \pm 4.02) \cdot 10^{-3}$	$(3.82 \pm 1.31) \cdot 10^{-3}$

One may assume naively that \overline{UV} will not depend on telescope offsets (X, Y) significantly, expecting that conditions of transfer for UV-photons will be close to ones for visible photons and, then, the ratio of photon numbers will be kept during propagation. But actually, there are also (as well as in case of

Table 4: Mean values and mean square deviations of the UV -parameter for the cosmic ray protons

Energy, TeV	31.62	100	316.2
(x, m; y, m)			
(-180; 0)	$(4.66 \pm 2.26) \cdot 10^{-2}$	$(4.94 \pm 1.55) \cdot 10^{-2}$	$(4.86 \pm 1.09) \cdot 10^{-2}$
(-150; 0)	$(3.99 \pm 1.98) \cdot 10^{-2}$	$(4.08 \pm 1.52) \cdot 10^{-2}$	$(4.01 \pm 1.05) \cdot 10^{-2}$
(-120; 0)	$(3.76 \pm 1.7) \cdot 10^{-2}$	$(3.22 \pm 1.15) \cdot 10^{-2}$	$(3.30 \pm 1.07) \cdot 10^{-2}$
(-90; 0)	$(4.96 \pm 2.37) \cdot 10^{-2}$	$(4.09 \pm 1.3) \cdot 10^{-2}$	$(3.55 \pm 0.93) \cdot 10^{-2}$
(0; 0)	$(1.99 \pm 1.2) \cdot 10^{-2}$	$(1.69 \pm 1.16) \cdot 10^{-2}$	$(1.76 \pm 1.06) \cdot 10^{-2}$
(90; 0)	$(4.8 \pm 2.64) \cdot 10^{-2}$	$(4.3 \pm 1.47) \cdot 10^{-2}$	$(3.67 \pm 0.97) \cdot 10^{-2}$
(120; 0)	$(3.72 \pm 1.62) \cdot 10^{-2}$	$(3.12 \pm 1.11) \cdot 10^{-2}$	$(3.14 \pm 1.03) \cdot 10^{-2}$
(150; 0)	$(3.67 \pm 1.95) \cdot 10^{-2}$	$(3.79 \pm 1.51) \cdot 10^{-2}$	$(3.81 \pm 1.09) \cdot 10^{-2}$
(180; 0)	$(4.41 \pm 2.19) \cdot 10^{-2}$	$(4.64 \pm 1.64) \cdot 10^{-2}$	$(4.54 \pm 1.08) \cdot 10^{-2}$
(0; 0)	$(19.9 \pm 12) \cdot 10^{-3}$	$(16.9 \pm 11.6) \cdot 10^{-3}$	$(17.6 \pm 10.6) \cdot 10^{-3}$
(0; 90)	$(16.1 \pm 6.5) \cdot 10^{-3}$	$(10.8 \pm 3.1) \cdot 10^{-3}$	$(8.7 \pm 1.82) \cdot 10^{-3}$
(0; 120)	$(13.3 \pm 6.4) \cdot 10^{-3}$	$(7.85 \pm 2.79) \cdot 10^{-3}$	$(5.98 \pm 1.25) \cdot 10^{-3}$
(0; 150)	$(10.9 \pm 5.8) \cdot 10^{-3}$	$(6.78 \pm 2.98) \cdot 10^{-3}$	$(5.33 \pm 1.84) \cdot 10^{-3}$
(0; 180)	$(12.6 \pm 8.1) \cdot 10^{-3}$	$(7.87 \pm 3.72) \cdot 10^{-3}$	$(6.46 \pm 2.53) \cdot 10^{-3}$

\overline{UV} -parameter in XY-plane. These reasons are similar to ones leading to surface \overline{Size} -distribution asymmetry but have additional features:

1) Asymmetric order of camera filling with filters (see Fig. 3) and definition (1) of the UV -value lead to the following effect: a) in case of telescope shift along X-axis, the pixels hit by first and second maximal numbers of Cherenkov photons will be masked by filters of different types (due to alternation of filter types along x -camera axis) with high probability; b) in case of telescope shift along Y-axis, the pixels hit by first and second maximal numbers of Cherenkov photons will be masked by filters of the same type (due to the same filter types along y -camera axis) with high probability. This will lead to asymmetry of surface \overline{UV} -distribution relative to X and Y axes of about order of magnitude, that is much more expressed than for \overline{Size} .

2) The strong dependence of Rayleigh scattering on photon wavelength ($\sim \lambda^{-4}$) leads to the following effect: the UV-photons are scattered much more intensively than visible photons (corresponding Rayleigh scattering coefficient in MUV range is from $\simeq 1.7 \cdot 10^{-4} \text{ m}^{-1}$ at 290 nm to $\simeq 3.2 \cdot 10^{-4} \text{ m}^{-1}$ at 250 nm, see e.g. Bucholtz 1995). As a result of that, the ring-like region containing the most of generated Cherenkov photons (in our calculations $r = 120, 150 \text{ m}$) becomes relatively impoverished with UV-photons while in the outside region and internal circle the relative enrichment of UV-ratio is observed.

3) As mentioned above, the inclination of EAS leads to different values of slant depth on Rayleigh scattering for Cherenkov photons coming to observation surface with positive and negative values of coordinate X. But due to strong dependence of Rayleigh scattering on photon wavelength this difference for (UVB+MUV) photons is larger on average than for the (visible+NUV) photons. Corresponding contribution to relative difference between \overline{UV} -values in points X and $-X$ can be estimated as $\delta_R^{UV} \simeq -2 \left(\overline{\Lambda}_R^{UV} - \overline{\Lambda}_R^{vis} \right) X \sin \Theta$,

– 320 nm and 290 – 590 nm respectively. The relative difference, δ_R^{UV} , may achieve $\sim -8\%$ for distant observation points $X = \pm 180$ m.

4) The inclination of EAS also leads to different values of slant depth on ozone absorption for Cherenkov photons coming to observation surface with positive and negative values of coordinate X . Corresponding contribution to relative difference between \overline{UV} -values in points X and $-X$ can be estimated as $\delta_{O_3}^{UV} \simeq -2\Lambda_{O_3} X \sin \Theta$, where Λ_{O_3} is ozone absorption coefficient near Earth surface, which can be estimated at a level values from $\sim 10^{-5} \text{ m}^{-1}$ at 300 nm up to $\sim 10^{-3} \text{ m}^{-1}$ at 260 nm to (based on crosssection given by Burrows et al. (1999); Orphal (2003)). The relative difference, $\delta_{O_3}^{UV}$, may achieve $\sim -5\%$ for distant observation points $x = \pm 180$ m.

To see from the $\overline{UV} \pm \sigma_{UV}$ data how effective the gamma-hadron separation can be, one may use the following simple and natural measure of distribution separation (“distance” between distributions):

$$\Delta_k^i = \frac{(\overline{UV}_i - \overline{UV}_k)}{(\sigma_{UV,i}^2 + \sigma_{UV,k}^2)^{1/2}} \quad (3)$$

where indecies i, k stand for distribution parameters (particle type, particle energy and others). Results of calculations of values Δ_k^i are presented in Tab. 5.

Table 5: Measure of separation of UV -distributions for CR protons and gamma-quanta

(x, m; y, m)	$\Delta_{\gamma 10}^{p31}$	$\Delta_{\gamma 31}^{p31}$	$\Delta_{\gamma 31}^{p100}$	$\Delta_{\gamma 100}^{p100}$
(-180; 0)	0.513	0.219	0.409	0.095
(-150; 0)	0.711	0.521	0.669	0.367
(-120; 0)	0.822	0.97	0.918	0.651
(-90; 0)	0.053	0.401	0.13	0.882
(0; 0)	0.94	1.13	0.916	0.847
(90; 0)	0.083	0.142	-0.022	0.74
(120; 0)	0.746	1.03	0.93	0.755
(150; 0)	0.702	0.508	0.666	0.386
(180; 0)	0.583	0.303	0.47	0.144
<hr/>				
(0; 0)	0.94	1.13	0.916	0.847
(0; 90)	0.675	1.57	1.47	1.89
(0; 120)	0.477	1.43	1.23	1.58
(0; 150)	0.173	1.13	0.781	1.28
(0; 180)	0.156	0.814	0.48	1.03

The general idea of using of measure (3) is the following: the larger the measure value the better the distribution separation and expected efficiency of gamma-hadron separation. Some deviations from this general tendence can be connected with the fact that actual UV -distributions are not Gaussian ones (and even not two-parametric ones). Despite these deviations one can make, for example, the following evident assumptions: if $\Delta_k^i \lesssim 0.2$ (these values are highlighted in Tab. 5 by red font) then the UV gamma-hadron separation will be almost impossible (since corresponding UV -distributions are overlapped strongly), if

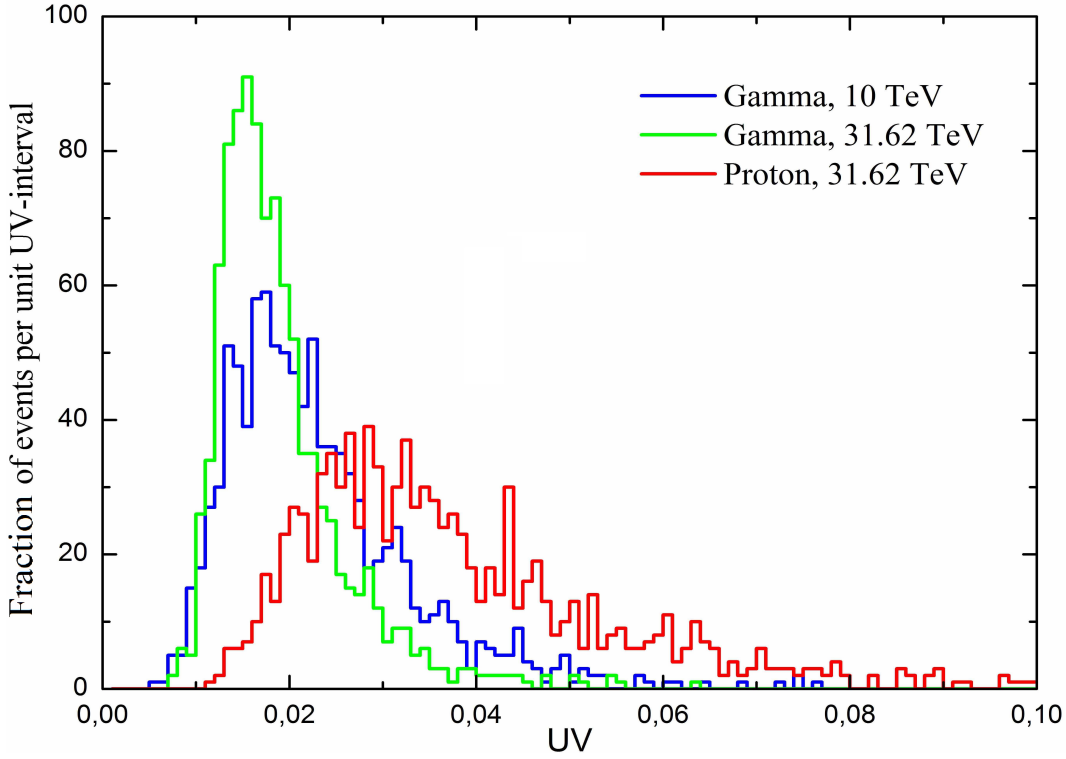


Figure 4: Distribution of the UV parameter for events induced by 10 TeV (blue curve) and 31.62 TeV (green curve) gamma-quanta and by 31.62 TeV protons (red curve) at observation point (120 m; 0 m).

UV -distribution are well-separated). In accordance with these assumptions, the results presented in Tab. 5 show that UV gamma-hadron separation may be effective in the interval of distances $\sim [120; 150]$ m at telescope offset along X axis relative to EAS axis, and for all considered distances (excepting large distances for $\Delta_{\gamma_{10}}^{p_{31}}$) at telescope offset along Y axis relative to EAS axis. Examples of explicit view of separation of UV -distributions for 10 and 31.62 TeV γ -quanta and 31.62 TeV protons at observation points (120 m; 0 m) and (0 m; 120 m) are presented in Fig. 4 and 5 respectively. The UV -distributions (the fractions of events per unit UV -interval, $f(UV)$) are normalized by the condition $\int f(UV) dUV = 1$.

Demanding only two parameters of UV -distribution, the calculation of separation measure (3) is the method for fast estimate of expected effectiveness of UV gamma-hadron separation for specific values of particle parameters. This method allows one to save the computer resources by rejecting exact calculations for obviously-ineffective variants of particle parameters⁶.

Finally the efficiency of gamma-hadron separation is characterized by the quality factor Q . This factor shows the increase of the signal confidence level due to a particular selection criterion in comparison with the confidence level without selection (*ceteris paribus*) and is given by the following formula:

$$Q = \kappa_{\gamma} / \kappa_p^{1/2}, \quad (4)$$

where κ_{γ} and κ_p are the acceptances of gamma- and proton-events, correspondingly (i.e. the fractions of selected events). These values can be calculated as follows:

$$\kappa_i (UV \leq UV_{cr}) = \int_0^{UV_{cr}} f_i(UV) dUV, \quad (5)$$

⁶ But in our simulations exact calculations for the full set of initial parameters are performed to state the correspondence between

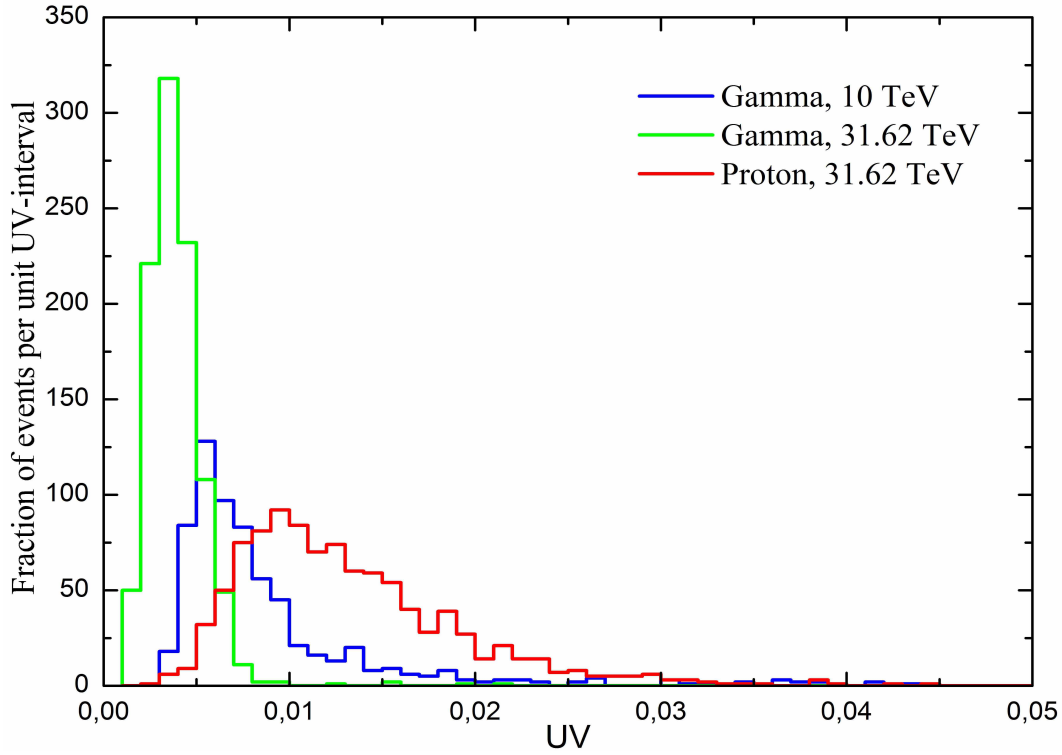


Figure 5: Distribution of the UV parameter for events induced by 10 TeV (blue curve) and 31.62 TeV (green curve) gamma-quanta and by 31.62 TeV protons (red curve) at observation point (0 m; 120 m).

where subscript i takes values “ γ ” and “p”, UV_{cr} is the UV -threshold defining a selection criterion.

The Q -factors have been calculated by maximization of value of expression (4) at variation of UV_{cr} with additional condition $\kappa_p \geq 0.025$. The latest is needed to provide stability of numerical results, because at small absolute values of κ_p its relative numerical deviations may become very large, that, correspondingly, leads to large deviations of calculated Q -values. The results of calculations of acceptances κ and corresponding maximal Q -factors, Q_{max} , for different values of particle energies and observation points are presented in Tab. 6 – 9. There are several typical cases:

a) In many cases, the maximum is very flat: the relative width $\Delta UV_{cr}/UV_{cr}^{max}$ is much larger than 0.1 (typically ~ 0.5) at level of $0.95Q_{max}$. In this case the intervals of parameters, corresponding to $\sim [0.95Q_{max}; Q_{max}]$, are shown in the tables. The value of UV_{cr} corresponding to Q_{max} is approximately at the middle of interval shown in tables. Specific values of selection criterion UV_{cr} can be chosen from additional reasonings, e.g. maximization of κ_γ or minimization of κ_p or other conditions arising from demands of Hillas analysis.

b) In most cases, Q -factors achieve the maximal values at “boundary” condition $\kappa_p \geq 0.025$ (i.e. the next step to decrease UV_{cr} leads to $\kappa_p < 0.025$). These values are marked by superscript “*” in Tab. 6 – 9.

c) In some cases, Q -factors achieve global maximum values (including case when this is actually achieved at $\kappa_p = 0.025$) and these maxima are expressive (i.e. sharp enough). These values are not marked by any additional indices.

d) In some cases, Q -factors remain below unity at all values of UV_{cr} . In these cases, values of selection

Table 6: Quality factor, Q , of separation between 10 TeV gamma-quanta and 31.62 TeV proton.

(x, m; y, m)	UV_{cr}	κ_γ	κ_p	Q
(-180; 0)	0.026 – 0.067	0.409 – 0.965	0.133 – 0.756	1.11 – 1.17
(-150; 0)	0.014 – 0.022	0.232 – 0.565	0.025 – 0.151	1.46 – 1.54
(-120; 0)	0.016	0.308	0.03	1.78*
(-90; 0)	–	–	–	<1
(0; 0)	0.007	0.515	0.028	3.08*
(90; 0)	–	–	–	<1
(120; 0)	0.017	0.298	0.032	1.67*
(150; 0)	0.014	0.308	0.032	1.72*
(180; 0)	0.024 – 0.048	0.461 – 0.893	0.155 – 0.594	1.16 – 1.22
(0; 0)	0.007	0.515	0.028	3.08*
(0; 90)	0.007	0.257	0.027	1.56
(0; 120)	0.006	0.232	0.048	1.06
(0; 150)	–	–	–	<1
(0; 180)	–	–	–	<1

Table 7: Values of quality factor, Q , of separation between 31.62 TeV gamma-quanta and 31.62 TeV proton.

(x, m; y, m)	UV_{cr}	κ_γ	κ_p	Q
(-180; 0)	0.054 – 0.1	0.804 – 1	0.599 – 0.961	1.03 – 1.08
(-150; 0)	0.027 – 0.05	0.587 – 0.929	0.28 – 0.711	1.1 – 1.16
(-120; 0)	0.016	0.388	0.03	2.24*
(-90; 0)	0.027	0.262	0.026	1.63*
(0; 0)	0.007	0.756	0.028	4.52*
(90; 0)	0.037 – 0.097	0.419 – 0.993	0.142 – 0.847	1.08 – 1.14
(120; 0)	0.017	0.478	0.032	2.67*
(150; 0)	0.025 – 0.034	0.625 – 0.822	0.285 – 0.512	1.15 – 1.21
(180; 0)	0.045 – 0.088	0.762 – 0.999	0.546 – 0.945	1.03 – 1.08
(0; 0)	0.007	0.756	0.028	4.52*
(0; 90)	0.007	0.833	0.027	5.07*
(0; 120)	0.006	0.929	0.048	4.24*
(0; 150)	0.005	0.871	0.059	3.59*
(0; 180)	0.004	0.415	0.025	2.63

The calculations show that measurements of the UV parameter at an offset $|X| \simeq 120$ m from the

Table 8: Values of quality factor, Q , of separation between 31.62 TeV gamma-quanta and 100 TeV proton.

(x, m; y, m)	UV_{cr}	κ_γ	κ_p	Q
(-180; 0)	0.045 – 0.071	0.666 – 0.957	0.438 – 0.892	1.01 – 1.054
(-150; 0)	0.021 – 0.027	0.334 – 0.587	0.06 – 0.188	1.36 – 1.43
(-120; 0)	0.017	0.462	0.028	2.76*
(-90; 0)	–	–	–	<1
(0; 0)	0.007	0.756	0.044	3.6*
(90; 0)	–	–	–	<1
(120; 0)	0.018	0.548	0.044	2.61*
(150; 0)	0.018	0.304	0.038	1.56*
(180; 0)	0.030 – 0.050	0.411 – 0.816	0.154 – 0.632	1.03 – 1.09
(0; 0)	0.007	0.756	0.044	3.6*
(0; 90)	0.006	0.666	0.034	3.61*
(0; 120)	0.004	0.589	0.032	3.29*
(0; 150)	0.004	0.701	0.092	2.31*
(0; 180)	0.004	0.415	0.056	1.75*

Table 9: Values of quality factor, Q , of separation between 100 TeV gamma-quanta and 100 TeV proton.

(x, m; y, m)	UV_{cr}	κ_γ	κ_p	Q
(-180; 0)	0.059 – 0.090	0.829 – 1	0.688 – 1	1 – 1.04
(-150; 0)	0.044 – 0.074	0.814 – 1	0.655 – 0.98	1.01 – 1.057
(-120; 0)	0.017	0.255	0.028	1.52*
(-90; 0)	0.024	0.356	0.038	1.83*
(0; 0)	0.007	0.694	0.044	3.31*
(90; 0)	0.024	0.247	0.03	1.43*
(120; 0)	0.018	0.408	0.044	1.94*
(150; 0)	0.032 – 0.1	0.64 – 1	0.404 – 1	1 – 1.05
(180; 0)	0.060 – 0.092	0.893 – 1	0.79 – 1	1 – 1.04
(0; 0)	0.007	0.694	0.044	3.31*
(0; 90)	0.006	0.925	0.034	5.02*
(0; 120)	0.004	0.875	0.032	4.89*
(0; 150)	0.004	0.928	0.092	3.06*
(0; 180)	0.004	0.656	0.056	2.77*

factor $Q \simeq 1.67 – 2.67$ under the criterion $UV \leq 0.017$. For higher energies the calculations show that a measurement of the UV parameter at the same offset allows one to separate 100 TeV protons from 31.62 TeV and 100 TeV γ -quanta with a quality factor $Q \simeq 1.52 – 2.76$ under the criterion $UV \leq 0.017$. The values of Q -factor drop as distance to EAS axis increases (at distances larger than 120 m), but at offset $|X| \simeq 150$ m most of these values remain acceptable enough: $Q \simeq 1.05 – 1.72$ depending on particle energy. At offset $|X| \simeq 180$ m, the values of Q -factor drop below $\simeq 1.2$ and UV gamma-hadron separation

For offsets along Y axis, the estimated Q-factors are significantly higher (excepting $Q_{\gamma 10}^{p31}$ for $|Y| \geq 120$ m) and take values in the interval 1.56 – 5.07. At that 12 of 18 estimated values are larger than 3, that says about very high potential efficiency of UV gamma-hadron separation for particles incident with offset along Y axis relative to the telescope position.

Here it should be emphasized once again that Q-factors are calculated as functions of telescope coordinates relative to the EAS axis. In general the Q-factors (for different types of gamma-hadron separation) can be calculated for specific values of distance (see e.g. Razdan et al. 2002) to EAS axis or for specific intervals of distance (i.e. averaged over the intervals, see e.g. Chitnis & Bhat 2001; Postnikov et al. 2017; Kunnas 2017). But Q-factor averaged over some interval of distance is naturally less than its peak values. Thus, if one can determine the distance with appropriate accuracy then the use of Q-factor as a function of distance (or averaged over narrow bins of distance) is preferable to achieve the more efficient separation where possible and to avoid the use of specific gamma-hadron separation where it is inefficient (i.e. at $Q < 1$). Also, full (as possible) dependence of Q-factor on distance allows one to obtain the averaged Q-factors for distance intervals of any required size, while the inverse operation is impossible in general. Thus, the use of considered scenario of UV gamma-hadron separation demands determination of the EAS axis position as correct as possible⁷. This, in turn, demands analysis of classical Hillas parameters (Hillas 1985) for considered camera configuration (with SiPM-pixels masked by filters of two different types). Taking into account that the analysis of Hillas parameters can be performed at $Size \gtrsim 100 - 120$ p.e. without doubts, the typical values of $Size$ estimated in the present paper for 10 TeV γ -EASs (see Tab. 1) and 31.62 TeV p-EASs (see Tab. 2) allow one to assume that this analysis will be possible at TAIGA IACT with camera of considered configuration at energies of primary particles larger than 3 – 4 TeV. This, in turn, opens a possibility to use the stereoscopic mode (if there are two or more IACTs in the observatory, which is valid for TAIGA IACT array) to improve some characteristics of observatory (for example, angular resolution). The detailed investigations of efficiency of analysis of Hillas parameters and operation in stereoscopic mode for considered camera configuration are beyond the scope of the present paper and will be considered in the next papers.

Obtained values of Q-factor are comparable with typical quality factors of gamma-hadron separation performed by analysis of single or pair of Hillas parameters (*length* and *width*) for small-size Cherenkov telescopes (see, e.g., Razdan et al. 2002; Postnikov et al. 2018) and, in some cases, exceed them significantly. This makes UV gamma-hadron separation a perspective method to improve sensitivity of small-size Cherenkov telescopes. Here it is relevant to note that both Hillas and UV gamma-hadron separations are directed to the same aim (selection of gamma-quanta from whole set of observed particles), and both methods have significant estimated efficiency (if taking into account the results of the present paper on efficiency of UV gamma-hadron separation). This allows to assume the presence of some correlation between UV-parameter and Hillas parameters *length* and *width*. The detailed estimate of this possible correlation is also beyond the scope of the present paper and will be investigated in the next papers.

For convenient comparison of Q-factors with separation measure (3), the maximal calculated Q-values only have been collected together in the cumulative table 10 (i.e. without intervals, additional indecies and comments).

Table 10: Cumulative table of Q-factors of UV gamma-hadron separation

(x, m; y, m)	$Q_{\gamma 10}^{p31}$	$Q_{\gamma 31}^{p31}$	$Q_{\gamma 31}^{p100}$	$Q_{\gamma 100}^{p100}$
(-180; 0)	1.17	1.08	1.054	1.04
(-150; 0)	1.54	1.16	1.43	1.057
(-120; 0)	1.78	2.24	2.76	1.52
(-90; 0)	<1	1.63	<1	1.83
(0; 0)	3.08	4.52	3.6	3.31
(90; 0)	<1	1.14	<1	1.43
(120; 0)	1.67	2.67	2.61	1.94
(150; 0)	1.72	1.21	1.56	1.05
(180; 0)	1.22	1.08	1.09	1.04
(0; 0)	3.08	4.52	3.6	3.31
(0; 90)	1.56	5.07	3.61	5.02
(0; 120)	1.06	4.24	3.29	4.89
(0; 150)	<1	3.59	2.31	3.06
(0; 180)	<1	2.63	1.75	2.77

Comparison of data of Tab. 5 and Tab. 10 shows that separation measure (3) allows one to predict expected level of Q-factor qualitatively. At $\Delta_k^i < 0.3$ all calculated values of Q-factor are less than 1.2, which means that UV gamma-hadron separation in these cases is ineffective. At $\Delta_k^i \geq 0.3$ one may note approximated relation $Q_k^i \simeq (2 - 4)\Delta_k^i$. This, for example means that at $\Delta_k^i = 0.7$ the expected value of Q-factor can be estimated as $\gtrsim 1.4$, which means that UV gamma-hadron separation in these cases is effective enough.

4 CONCLUSION

With multi-particle Monte Carlo simulations of performance of a small-size Cherenkov gamma-ray telescope TAIGA-IACT equipped with modern SiPM detectors and two types of optical filters it is shown that the fraction of middle UV emission in the total amount of the detected Cherenkov signal can be efficiently used for gamma-hadron separation of the energetic primaries. In particular, measurements of only one UV-parameter at observation of Crab gamma-ray source would lead to primary type separation with quality factor $1.05 \lesssim Q \lesssim 2.76$ at offsets 120 – 150 m along axis of camera filter alternation in the energy range 10 – 100 TeV. Along perpendicular axis the quality factor is $1.75 \lesssim Q \lesssim 5.07$ at offsets 0 – 180 m in the energy range 31 – 100 TeV and $1.06 \lesssim Q \lesssim 5.07$ at offsets 0 – 120 m in the energy range 10 – 100 TeV. Hence, gamma-hadron separation based on the UV-parameter analysis can be considered as one of

In addition the dependencies of *Size*-parameter on particle energy for gamma-quanta and CR protons have been obtained specifically for the configuration of TAIGA-IACT equipped with SiPM detectors and two types of optical filters. These dependencies are necessary for possibility of determination of particle energy from observable quantity *Size*, and will be useful for further simulations of EAS observations with this configuration of telescope.

Financial support

The modeling by A. B. was supported by grant of the Ministry of Science and Higher Education of the Russian Federation 23-075-67362-1-0409-000105. The work of A. K. and E. Kh. was supported by the baseline project FFUG-2024-0002 at the Ioffe Institute. The work of N. B. was supported by the baseline projects FZZE-2023-0004 and FZZE-2024-0005 at the Irkutsk State University.

Conflict of interests

The authors declare no conflicts of interest.

References

- Adams, C. B., Alfaro, R., Ambrosi, G., et al. 2021, *Astroparticle Physics*, 128, 102562 2
- Aharonian, F. A., Hofmann, W., Konopelko, A. K., & Völk, H. J. 1997, *Astroparticle Physics*, 6, 343 2
- Aharonian, F. A., Akhperjanian, A. G., Kankanian, A. S., et al. 1991, in *International Cosmic Ray Conference*, Vol. 2, *International Cosmic Ray Conference*, 615 1
- Anderhub, H., Backes, M., Biland, A., et al. 2011, *Nuclear Instruments and Methods in Physics Research A*, 639, 58 2
- Ansoldi, S., Antonelli, L. A., Antoranz, P., et al. 2016, *Astronomy & Astrophysics*, 585, A133 2
- Antonov, A. S., Bogdanov, A. A., Krassiltchikov, A. M., & Kholupenko, E. E. 2024, *Journal of Technical Physics*, 68, 505 7
- Benn, C. R., & Ellison, S. L. 1998, *New Astronomy Reviews*, 42, 503 3, 4, 6, 7
- Bogdanov, A. A., Repman, G. A., Tubol'tsev, Y. V., et al. 2022, to be submitted to *Journal of Physics Conference Series* 2
- Bogdanov, A. A., Tubol'tsev, Y. V., Chichagov, Y. V., Kholupenko, E. E., & Krasil'shchikov, A. M. 2021a, *Journal of Technical Physics*, 66, 699 2
- Bogdanov, A. A., Tuboltsev, Y. V., Chichagov, Y. V., & Krassilchtchikov, A. M. 2021b, *Journal of Physics: Conference Series*, 2103, 012026 2
- Bogdanov, A. A., Tuboltsev, Y. V., Chichagov, Y. V., et al. 2020, in *Journal of Physics Conference Series*, Vol. 1697, *Journal of Physics Conference Series*, 012015 2
- Bretz, T., Anderhub, H., Backes, M., et al. 2014, *arXiv e-prints*, arXiv:1403.3573 2
- Bucholtz, A. 1995, *Applied Optics LP*, 34, 2765 10, 11
- Budnev, N., Astapov, I., Bezyazeev, P., et al. 2022, *Nuclear Instruments and Methods in Physics Research A*, 1039, 167047 2, 3
- Burrows, J. P., Richter, A., Dehn, A., et al. 1999, *Journal of Quantitative Spectroscopy and Radiative Transfer*, 61, 509 12

- Bykov, A. M., Aharonian, F. A., Krassilchtchikov, A. M., et al. 2017, *Journal of Technical Physics*, 62, 819 1
- Charman, W. N., D. R. W. P. 1969, *Nature*, 224, 567 2
- Chitnis, V. R., & Bhat, P. N. 2001, *Astroparticle Physics*, 15, 29 17
- Cummings, A. L., Aloisio, R., Eser, J., & Krizmanic, J. F. 2021, *Phys. Rev. D*, 104, 063029 9
- Ergin, M. S. T. 2005, *The Energy Spectrum of Very High Energy Gamma Rays from the Crab Nebula as Measured by the H.E.S.S. Array*, dissertation, Humboldt-Universitat zu Berlin 17
- Fegan, D. J., McBreen, B., O'Mongain, E. P., Porter, N. A., & Slevin, P. J. 1968, *Canadian Journal of Physics Supplement*, 46, 433 1
- Giller, M., Wieczorek, G., Kacperczyk, A., Stojek, H., & Tkaczyk, W. 2004, *Journal of Physics G Nuclear Physics*, 30, 97 9
- Gottschall, D., Förster, A., Bonardi, A., Santangelo, A., & Puehlhofer, G. 2015, in *International Cosmic Ray Conference*, Vol. 34, 34th International Cosmic Ray Conference (ICRC2015), 1017 1
- Hanna, D., O'Brien, S., & Rosin, T. 2022, *Nuclear Instruments and Methods in Physics Research A*, 1027, 166235 1
- Heck, D., Knapp, J., Capdevielle, J. N., Schatz, G., & Thouw, T. 1998, *CORSIKA: a Monte Carlo code to simulate extensive air showers*. (Forschungszentrum Karlsruhe GmbH, Karlsruhe (Germany)), V + 90 p., TIB Hannover, D-30167 Hannover (Germany)) 6
- Hillas, A. M. 1985, in *International Cosmic Ray Conference*, Vol. 3, 19th International Cosmic Ray Conference (ICRC19), Volume 3, 445 2, 17
- Hofmann, W., & H. E. S. S. Collaboration. 2003, in *International Cosmic Ray Conference*, Vol. 5, International Cosmic Ray Conference, 2811 2
- Holder, J., Acciari, V. A., Aliu, E., et al. 2008, in *American Institute of Physics Conference Series*, Vol. 1085, American Institute of Physics Conference Series, ed. F. A. Aharonian, W. Hofmann, & F. Rieger, 657 1
- Homola, P., Engel, R., & Wilczyński, H. 2015, *Astroparticle Physics*, 60, 47 9
- Kalekin, O. R., Neshpor, Y. I., Stepanyan, A. A., et al. 1995, *Astronomy Letters*, 21, 163 2
- Kholupenko, E. E., Bykov, A. M., Aharonian, F. A., et al. 2018, *Journal of Technical Physics*, 63, 1603 2, 6
- Kholupenko, E. E., Krassilchtchikov, A. M., Badmaev, D. V., & Bogdanov, A. A. 2024, *Bulletin of the Russian Academy of Sciences, Physics*, 88, 427 7
- Kholupenko, E. E., Krassilchtchikov, A. M., Badmaev, D. V., et al. 2020, *Journal of Technical Physics*, 65, 886 7
- Kholupenko, E. E., Badmaev, D. V., Antonov, A. S., et al. 2022, *Journal of Technical Physics*, 67, 80 6, 7
- Kneizys, F. X., Abreu, L. W., Anderson, G. P., et al. 1996, *The MODTRAN 2/3 report and LOWTRAN 7 model*, ed. L. W. Abreu & G. P. Anderson (prepared for: Phillips Laboratory, Geophysics Directorate, Hanscom AFB, MA 01731, U.S.A.; prepared by: Ontar Corporation, 9 Village Way, North Andover, MA 01845) 6

- Knoetig, M. L., Biland, A., Bretz, T., et al. 2013, in International Cosmic Ray Conference, Vol. 33, International Cosmic Ray Conference, 1132 2
- Kuleshov, D. O., Simonyan, V. A., Bogdanov, A. A., et al. 2021, in Journal of Physics Conference Series, Vol. 2103, Journal of Physics Conference Series, 012036 2
- Kunnas, M. H. 2017, Studies of the performance of an IACT system for the TAIGA array, PhD thesis, der Fakultat für Mathematik, Informatik und Naturwissenschaften Fachbereich Physik der Universität Hamburg 17
- Kuzmichev, L. 2022, in 44th COSPAR Scientific Assembly. Held 16-24 July, Vol. 44, 2142 3
- Kuzmichev, L. A., Astapov, I. I., Bezyazeev, P. A., et al. 2018, Physics of Atomic Nuclei, 81, 497 3, 7
- Leinert, C., Bowyer, S., Haikala, L. K., et al. 1998, Astronomy and Astrophysics Supplement, 127, 1 3, 4, 6, 7
- Lombardi, S., Catalano, O., Scuderi, S., et al. 2020, Astronomy & Astrophysics, 634, A22 2
- Longo, F. 2022, in 44th COSPAR Scientific Assembly. Held 16-24 July, Vol. 44, 2387 2
- Lubsandorzhev, N., Astapov, I., Bezyazeev, P., et al. 2017, in International Cosmic Ray Conference, Vol. 301, 35th International Cosmic Ray Conference (ICRC2017), 757 7
- Manomenova, V. L., Rudneva, E. B., Voloshin, A. É., et al. 2005, Crystallography Reports, 50, 877 3, 7
- Mikhalev, A. V., & Medvedeva, I. V. 2002, Atmospheric and Oceanic Optics Journal, [in russian], 15, 902 3, 7
- Mikhalev, A. V., Medvedeva, I. V., Beletsky, A. B., & Kazimirovsky, E. S. 2001, Journal of Atmospheric and solar-terrestrial physics, 63, 865 3, 7
- Mirzoyan, R., & Lorenz, E. 1994, Internal report of the HEGRA collaboration. MPI-PhE/94-35 7
- Neshpor, Y. I., Chalenko, N. N., Stepanian, A. A., et al. 2001, Astronomy Reports, 45, 249 2
- ON-Semiconductor. 2017, J-Series SiPM Sensors. Silicon Photomultipliers (SiPM), High PDE and Timing Resolution Sensors in a TSV Package; <https://www.onsemi.com/pub/Collateral/MICROJ-SERIES-D.PDF>, ON Semiconductor 3, 7
- Orphal, J. 2003, Journal of Photochemistry and Photobiology A: Chemistry, 157, 185 12
- Postnikov, E. B., Grinyuk, A. A., Kuzmichev, L. A., & Sveshnikova, L. G. 2017, in European Physical Journal Web of Conferences, Vol. 145, European Physical Journal Web of Conferences, 19005 17
- Postnikov, E. B., Bychkov, I. V., Dubenskaya, J. Y., et al. 2018, arXiv e-prints, arXiv:1812.01551 2, 17
- Rahman, M. A., Bhat, P. N., Acharya, B. S., et al. 2001, Experimental Astronomy, 11, 113 2, 6
- Rahman, M. A., Bhat, P. N., Acharya, B. S., et al. 2002, Bulletin of the Astronomical Society of India, 30, 335 6
- Razdan, A., Haungs, A., Rebel, H., & Bhat, C. L. 2002, Astroparticle Physics, 17, 497 2, 6, 17
- Rudneva, E. B., Manomenova, V. L., & Voloshin, A. E. 2018, Crystallography Reports, 63, 1005 3, 7
- Stepanian, A. A., Fomin, V. P., & Vladimirkii, B. M. 1983, Izvestiya Ordena Trudovogo Krasnogo Znameni Krymskoj Astrofizicheskoy Observatorii, 66, 234 2
- Thébault, E., Finlay, C. C., Beggan, C. D., et al. 2015, Earth, Planets, and Space, 67, 79 6
- Tridon, D. B., Schweizer, T., Goebel, F., et al. 2010, Nuclear Instruments and Methods in Physics Research A, 623, 437 1

- Tsuchiya, K., Enomoto, R., Ksenofontov, L. T., et al. 2004, *The Astrophysical Journal Letters*, 606, L115 1
- van Eldik, C., Holler, M., Berge, D., et al. 2015, in *International Cosmic Ray Conference*, Vol. 34, 34th International Cosmic Ray Conference (ICRC2015), 847 2
- Vasiliev, R. V., Gress, O. A., Korosteleva, E. E., & et al. 2009, *Instrum. Exp. Tech.*, 52, 166 6
- Weekes, T. C., Cawley, M. F., Fegan, D. J., et al. 1989, *The Astrophysical Journal*, 342, 379 1, 2
- Zabudko, M. A. 2021, *Specifications of filters SL 280 – 390 and SL 290 – 590*, Photooptic Ltd. 3, 7
- Zyskin, Y. L., Vladimirsky, B. M., Neshpor, Y. I., et al. 1987, *International Cosmic Ray Conference*, 2, 342